Review Article

# Recent achievements using X-ray fluorescence holography and photoelectron holography

Atomic-resolution holography is a method of 3D atomic structure determination based on Gabor's original concept of holography. We are leading research on atomic-resolution holography with X-rays, electrons and neutrons. Among several types of atomic-resolution holography, X-ray fluorescence holography (XFH) [1, 2] and photoelectron holography (PH) have been conducted mostly at SPring-8, and many important achievements have been produced thus far. We show some recent results of XFH and PH in the present article.

In both XFH and PH, there are "normal" and "inverse" modes [2], as shown in Figs. 1(a) and 2(b), respectively. In the normal mode (Fig. 1(a)), fluorescent X-rays or photoelectrons from atoms in a sample, with and without being scattered by surrounding atoms, serve as the object and reference waves, respectively. A holographic pattern is recorded by scanning a detector around the sample. In the inverse mode (Fig. 1(b)), fluorescence (or characteristic X-rays) is used to detect an interference field originating from incident and scattered X-rays or electrons. The holographic pattern is obtained by detecting the fluorescence (or characteristic X-rays) while the sample's orientation is varied relative to the incident beam. XFH and PH are expected to be used for medium-range local structural analysis, which cannot be performed by X-ray diffraction or x-ray absorption fine structure analysis.

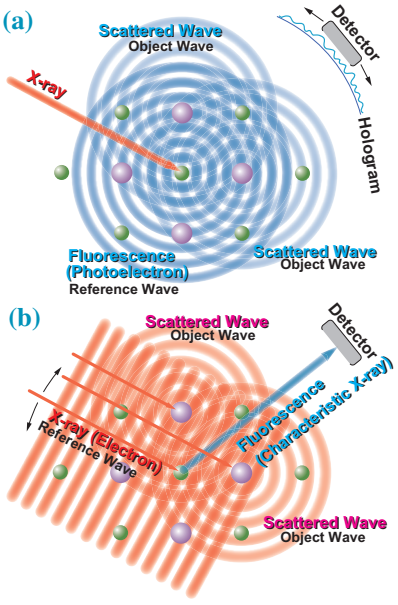


Fig. 1. Principle of atomic resolution holography. **(a)** Normal mode. **(b)** Inverse mode.

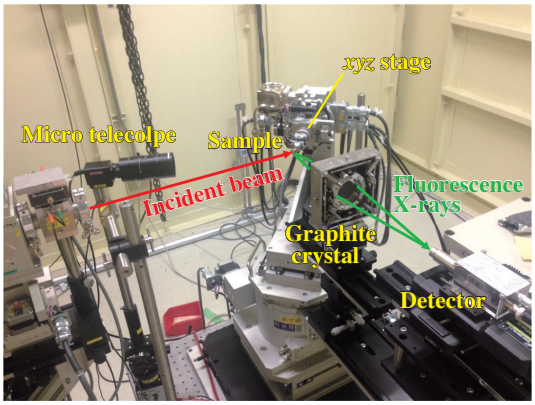


Fig. 2. Photograph of X-ray fluorescence holography apparatus.

## X-ray fluorescence holography

Figure 2 shows the XFH apparatus installed at SPring-8 BL13XU [3]. In the measurements of holograms in the inverse mode, the intensity variation of the X-ray fluorescence is measured as a function of the direction of the incident X-ray beam. Fluorescent photons from the sample should be detected as much as possible within the large solid angle of the detector. To accept and choose the wanted X-ray fluorescence lines with large solid angles, we have used cylindrical or toroidal graphite analyzers. The energy-analyzed fluorescent photons are focused on an avalanche photodiode (APD), which is a typical fast X-ray detector with a maximum count rate of as high as $10^8$ cps. On the other hand, a silicon drift detector, which is an energy-dispersive detector, has been recently used for dilute systems instead of avalanche photodiodes. In dilute systems, even when using the analyzing crystals, unwanted radiation is still detected at a non-negligible intensity ratio. Thus, further analysis of the incoming X-rays using the silicon drift detector is effective for measuring pure holograms. Typical scan ranges of azimuthal $\phi$ and incident $\theta$ angles are $0° \leq \phi \leq 360°$ in steps of 0.25° and $0° \leq \theta \leq 75°$ in steps of 1°, respectively. Regarding X-ray fluorescence holography, we describe here two applications to state-of-the-art metallic materials.

Mg alloys have attracted considerable attention owing to their lightness because we must reduce the energy

consumption of vehicles, such as cars, trains and airplanes. However, pure Mg is disadvantageous for its poor workability and low fire resistance. The Mg alloy with a synchronized long-period stacking ordered (LPSO) structure would be one of the solutions; it is a long-period stacking derivative of the hcp Mg structure, where the hcp structure is modified by a periodical insertion of stacking faults. The stacking fault is related to the concentration of heavier impurity elements, which form specific cluster structures, as shown in Fig. 3(a). Since the excellent mechanical properties of these Mg alloys are believed to originate from the synchronized LPSO structure, details of the LPSO structure have been investigated using various characterization methods. Here, we studied the local structure around Zn in the 10H-type long-period stacking ordered $Mg_{75}Zn_{10}Y_{15}$ alloy by XFH [4,5].

XFH measurements were performed at SPring-8 BL39XU. Using a focusing mirror and a slit, we obtained a small beam size of 20 × 20 $\mu m^2$, which serves to record fluorescent X-rays from a small single-crystal region of about 0.3 × 1.0 $mm^2$. In addition, the polycrystalline region of the sample was masked with Ag paste to suppress the emission of the fluorescent X-rays from the polycrystalline parts. We set the energies of the incident X-rays from 10.0 to 13.5 keV in steps of 0.25 keV and measured Zn Kα holograms. We can observe clear standing wave lines in the measured holograms, confirming that the measurements were successful.

As shown in Fig. 3(b), atomic images were clearly observed at 4.2 Å from the central Zn atom and correspond to Zn atoms inside the $L1_2$ cluster. On the other hand, the atomic images at the positions indicated by dashed circles are hardly observable, which correspond to those in the adjacent clusters. Figure 3(c) shows the reconstruction obtained from the calculated holograms using the structure model depicted in Fig. 3(a), and the dashed circles are superposed experimental results. This result indicates weak intercluster positional correlations. To evaluate the magnitude of the fluctuations, we calculated the atomic image including the positional fluctuation between the $L1_2$ clusters. A simulation including intercluster positional fluctuations with a magnitude of 0.33 Å well reproduced the experimental results. Because the degree of order is strongly related to the mechanical properties, the quantitative information of the intercluster fluctuation will be useful for understanding the origin of the excellent mechanical properties of LPSO alloys.

$Fe_2VAl$ Heusler-type alloy is a promising thermoelectric material consisting only of abundant elements. The performance of thermoelectric materials is expressed by the dimensionless figure of merit, $ZT = (S^2/\rho\kappa)T$, where T is the temperature, S is the Seebeck coefficient, ρ is the electrical resistivity, and κ is the thermal conductivity. The S value of this material is as high as that of the bismuth chalcogenide system, which is used in commercially available thermoelectric material, but, the κ value is larger than that of the bismuth chalcogenides by one order of magnitude. Therefore, reducing the thermal conductivity is an urgent issue that must be resolved to enable practical use. One solution is the doping of a heavy element, which scatters phonons, to reduce the thermal conductivity. On the basis of this idea, Nishino and his coworkers doped Ta into the V site and observed a significant effect on the thermal conductivity. To gain details on the local structure around Ta, we measured Ta *K*-edge X-ray fluorescence holograms of a Ta-doped $Fe_2VAl$ single crystal [6].

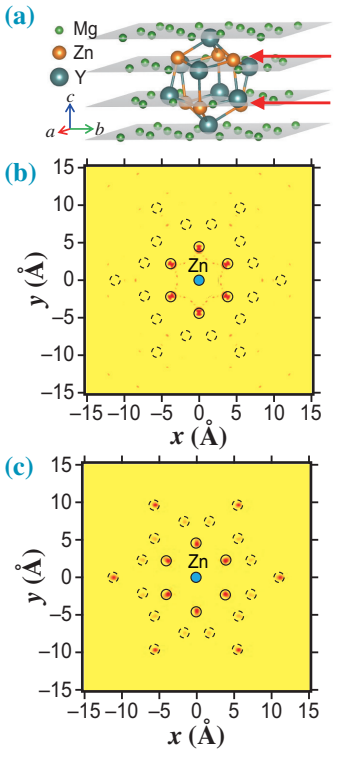


Fig. 3. Atomic images of (0001) planes around Zn in $Mg_{75}Zn_{10}Y_{15}$ alloy. **(a)** Atomic configuration of $Zn_6Y_8$ cluster. **(b)** Experimental data. **(c)** Calculated data. (b) and (c) show superpositions of neighbor Zr images on the same (0001) planes indicated by the coordinates in (a).

A $Fe_2(V_{0.95}Ta_{0.05})Al$ single crystal was prepared by the Czochralski method in a triarc furnace. XFH measurements were performed at SPring-8 BL13XU and BL6C at Photon Factory in Japan. We measured Ta Lα and V Kα holograms with the same incident X-ray energy range (11.9–14.4 keV in steps of 0.5 keV). The measured holograms of V Kα and Ta Lα show clear standing wave lines, indicating that the experiments were successfully performed. We also measured the X-ray absorption fine structure (XAFS) of $Fe_2(V_{0.95}Ta_{0.05})Al$ to determine more precisely the features of the local structure. Moreover, inelastic X-ray scattering (IXS) was applied to this material to understand the relationship between the doped Ta and the atomic dynamics.

The reconstructed atomic image of the Fe plane around V is shown in Fig. 4(a). Circles indicate the expected positions of Fe atoms around V, derived from the crystal structure of $Fe_2VAl$. Clear atomic images are observable within the circles. Figure 4(b) shows the corresponding atomic image around Ta. The positions of the spots agree well with those around V. On the other hand, the intensity of the atomic images is higher around Ta than around V. Such a feature was also observed

in the radial distribution functions (RDFs) around V and Ta obtained from XAFS measurement. This behavior is in contrast to the observation that atomic images around dopants exhibit a lower intensity than those around matrix elements. In addition, higher intensities around Ta were observed in a wide spatial range of more than 10 Å. These results show that the positional correlation between Ta and surrounding Fe atoms is much more rigid than that between V and Fe atoms. In the IXS results, we observed a broad dispersionless mode cross to the acoustic phonons, called the "resonant mode". It disturbs the coherency of phonons and thus will enhance the thermal insulation.

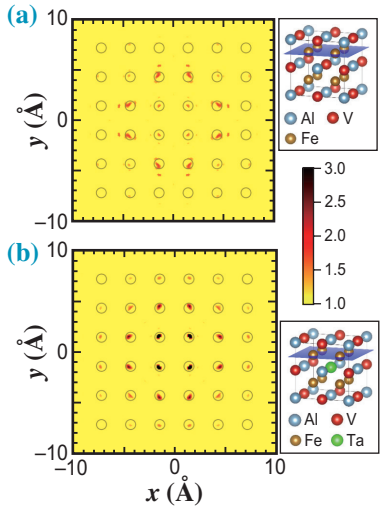


Fig. 4. Atomic images of Fe plane in Ta-doped $Fe_2VAl$ Heusler-type alloy. **(a)** Image around V. **(b)** Image around Ta. The right figures show $Fe_2VAl$ and Ta-doped $Fe_2Val$ structures, respectively. We sliced the images at the blue planes. The color bar indicates the image intensities.

## Photoelectron holography

Photoelectron holography is an advanced technology of core-level X-ray photoelectron spectroscopy (XPS). The atomic arrangement of the dopant can be determined, which is one of advantages of XPS measurement. The core-level XPS can identify the elements contained in the material. In addition, the valence state of the element can be directly observed because the binding energy shifts with the valence state (chemical shift). This feature enables us to distinguish holograms from different dopant sites even with the same element, which cannot be performed by other ordinary techniques. In addition, it is sensitive to surfaces and is useful for observing the chemical state of semiconductor circuits that are created on the surface and for tracking changes in the chemical state of catalysts that react on the surface. The principle of photoelectron holography can be explained using Fig. 1(a). Since the scattering power of electrons is larger than that of X-rays by two orders of magnitude, the holographic pattern of PH is more observable than that of XFH.

At SPring-8, some types of apparatus for photoelectron measurement have been installed, as shown in Fig. 5. The display-type spherical mirror analyzer (DIANA) shown in Fig. 5(a) has been in place since 1997. Since it can display the photoelectron angular distribution two-dimensionally in real time, it has supported the development of many photoelectron diffraction and holography techniques. Some examples are given below.

- Principle of photoelectron holography and demonstration of atomic image reconstruction theory [7]. This work mainly theoretically clarified the physics factors of the geometric patterns that appear in high-resolution photoelectron holograms.
- X-ray absorption and magnetic circular dichroism measurements of magnetic thin film, as shown in Fig. 6(a) [8]. It was shown that it is possible to perform layer-by-layer X-ray absorption and magnetic circular dichroism measurements on Ni thin films on a Cu substrate.
- Layered material such as graphene, as shown in Figs. 6(b,c) [9,10]. These studies revealed the atomic arrangement of graphene and buffer layers that can be obtained by heating SiC, and that of graphite showing superconductivity when doped with Ca and K.

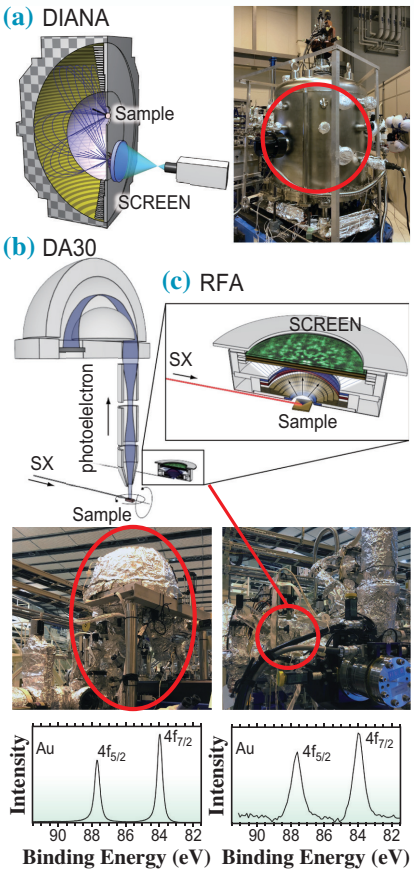


Fig. 5. Electron analyzers for photoelectron holography. **(a)** Display-type analyzer. **(b)** DA30. **(c)** RFA [12].

- Measurement of the reaction structure of the gas-sensing material W-doped ZnO as shown in Fig. 6(d) [11]. The atomic sites of the dopant W were clarified, and it was found that the W atoms migrate to the surface side by heat treatment.

The energy resolution used to be a bottleneck for the precise photoelectron holography measurement and the chemical shift could not be measured. Recently, the apparatus using the DA30 electron energy analyzer (Scienta Omicron) shown in Fig. 5(b) and the retarding field analyzer (RFA) [12] shown in Fig. 5(c) have been developed, and these have markedly improved the energy resolution. The RFA is a display-type electron energy analyzer like DIANA. As shown in Fig. 5(c), the energy resolution of the

RFA is slightly lower than that of the DA30 electron analyzer, but chemical shifts can be sufficiently separated. DA30, on the other hand, has a high energy resolution and can measure fine chemical shifts, as well as relatively low concentrations of dopants. However, the measurement time is long because the sample is measured while being rotated. The RFA is good choice for dopants at concentrations of a few at%, and DA30 is useful for more dilute dopants. Currently, there is a report of a measurement down to 0.06 at% obtained using DA30. As a result of measurements using DA30, the structure of the As dopant in Si crystal [13] and the structure of the P dopant in diamond [14] have been determined. With the improved energy resolution, it is now possible to separate the arrangement of each kind of atom in accordance with the chemical state of the dopant. In As in Si, a substitutional structure and an $As_2V$ structure (Fig. 6(e)) were observed. In P in diamond, a substitutional structure and a P$V$ split vacancy were observed (Fig. 6(f)). In addition, the structural anisotropy attributed to crystal growth was also observed. This information will be important in material fabrication. Photoelectron holography is expected to make great progress in the future.

In the XFH part, we showed the results for the LPSO Mg alloy and Heisler-type thermoelectric material. In the PH part, first we introduced the position-sensitive detectors of photoelectrons used in the experiments and then we showed PH applications to several materials. Both holography techniques have provided valuable information on local structures around dopants that help to understand the material functions. We look forward to welcoming new users reading this review to our community.

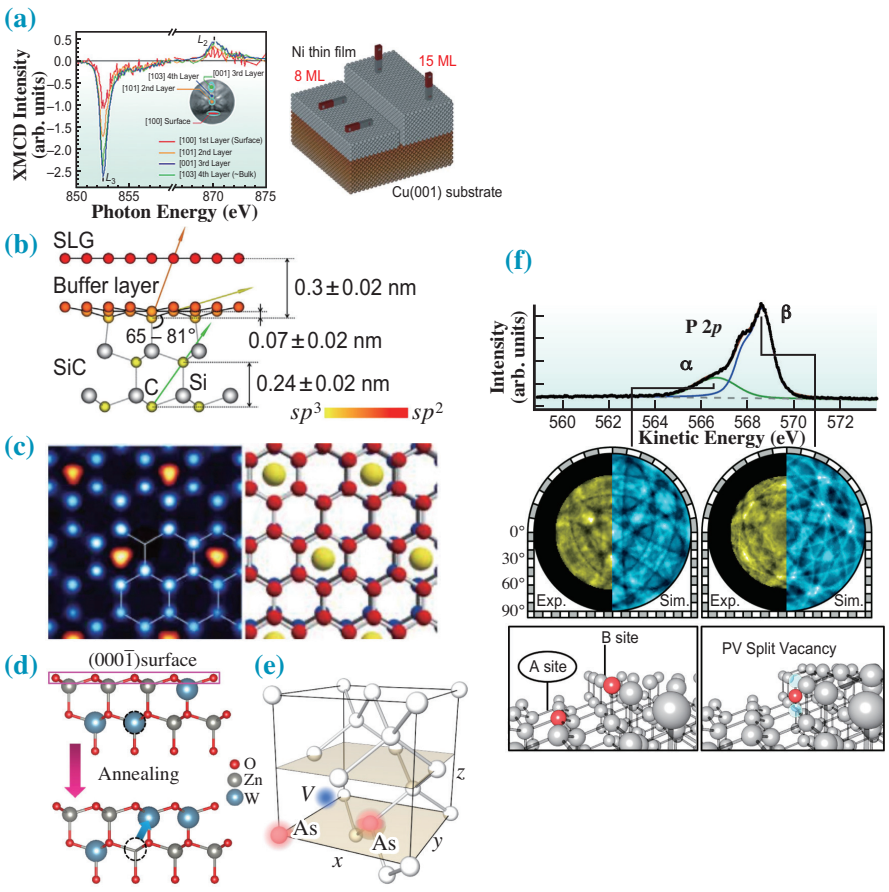


Fig. 6. Experimental results of photoelectron holography (diffraction). **(a)** Measurement of each atomic layer of Ni thin film [8]. The image on the left shows the MCD spectrum of each Ni atomic layer. The image on the right shows the direction of the magnetization in a Ni film. **(b)** Atomic structure of graphene grown on SiC [9] obtained from photoelectron hologram (diffraction). A buffer layer is formed under the graphene layer. **(c)** Atomic arrangement of intercalated K atoms in a layer of graphite [10] obtained from photoelectron hologram. The intercalant metal atom layer was found between two AA-stacked graphenes. The K atomic image revealed 2 × 2 periodicity. **(d)** W structure of the gas sensing material W-doped ZnO [11]. The dopant W atoms were found to occupy the Zn atom sites. Heat treatment caused W atoms to move to the surface side. **(e)** As dopant in Si crystal [13]. Not only substitution sites but also $As_2V$ structures with vacancies were observed, as shown in the figure. **(f)** P dopant in diamond crystal [14]. From the X-ray photoemission results, two components were found, and their photoelectron holograms (Exp.) were obtained. They were determined to be substitutional and PV split vacancy structures. Sim. are the results of photoelectron hologram simulations based on the atomic structures.

Kouichi Hayashi[a,*]
and Tomohiro Matsushita[b]

[a] Nagoya Institute of Technology
[b] Nara Institute of Science and Technology

*Email: hayashi.koichi@nitech.ac.jp

## References

[1] K. Hayashi and P. Korecki: J. Phys. Soc. Jpn. **87** (2018) 061003.
[2] K. Hayashi *et al.*: J. Phys. Condens. Matter. **24** (2012) 093201.
[3] N. Happo *et al.*: Jpn. J. Appl. Phys. **57** (2018) 058006.
[4] K. Kimura *et al.*: Mater. Trans. **58** (2017) 539.
[5] T. Nishioka *et al.*: Materialia **3** (2018) 256.
[6] K. Kimura *et al.*: Phys. Rev. B **101** (2020) 024302.
[7] T. Matsushita *et al.*: Phys. Status Solidi B **257** (2020) 2000117.
[8] F. Matsui *et al.*: Phys. Rev. Lett. **100** (2008) 207201.
[9] H. Matsui *et al.*: Surf. Sci. **635** (2015) 1.
[10] F. Matsui *et al.*: Sci, Rep. **6** (2016) 36258.
[11] S. Fukami *et al.*: Phys. Rev. App. **7** (2017) 064029.
[12] T. Muro *et al.*: Rev. Sci. Instrum. **88** (2017) 123106.
[13] K. Tsutsui *et al.*: Nano Lett. **17** (2017) 7533.
[14] T. Yokoya *et al.*: Nano Lett. **19** (2019) 5915.